Phase evolution and mechanical performance of an ettringite-based binder during hydrothermal aging

Hoang Nguyen [a],[*], Valter Carvelli [b], Wolfgang Kunther [c], Mirja Illikainen [a], Paivo Kinnunen [a]

[a] *Fibre and Particle Engineering Research Unit, University of Oulu, Pentti Kaiteran katu 1, 90014 Oulu, Finland*
[b] *Department A.B.C., Politecnico di Milano, Piazza Leonardo Da Vinci 32, 20133 Milan, Italy*
[c] *Department of Civil Engineering, Technical University of Denmark, 2800 Kgs. Lyngby, Denmark*

ARTICLE INFO

ABSTRACT

Little is known about the performance of ettringite-based binders in hydrothermal conditions. This investigation aims to gain insights into the phase evolution and corresponding mechanical performance of an ettringite-based binder considering crystallization pressure caused by late-reaction products. Additionally, the role of fiber reinforcement on the strength retention of the binder was investigated. When aged at an elevated temperature under water-saturated conditions, hard-burned MgO hydrated to form brucite. The precipitation and growth of the brucite crystals led to a crystallization pressure of approximately 200 MPa calculated using thermodynamic modelling. Damage was observed after 4 months of aging with cracks in the microstructure and eventually a failure at the macro scale. Ettringite remained stable at 60 °C due to the water-saturated conditions. Polypropylene fiber delayed crack propagation and thus reduced the damage caused by crystallization pressure. The fiber improved the flexural performance of composite attaining deflection-hardening behavior regardless of aging conditions.

1. Introduction

To reduce the carbon footprint of the cement industry, several pathways have been highlighted, including using alternative cementitious binders to partially replace conventional Portland cements (PC) [1–3]. Ettringite-based binders are one of several promising options that have been studied intensively in recent decades, and its advantages over PC have been proven via an approximately 24% reduction in CO_2 emissions while maintaining comparable performance [2,4]. The binders are formed as a result of the hydration between hydraulic Al-containing crystalline and/or amorphous phases and sulfate sources leading to the formation of ettringite as the main crystalline hydrate. The most investigated ettringite-based binders are calcium sulphoaluminate (CSA) cement and supersulfated cement (SSC). The former was introduced for the first time by Klein and Troxell in the 1950s [5], and is described as the third series cements in China [6], while the latter was first reported by Hans Kühl in 1908 [7].

The interest in alternative binders considerably increased when studies began focusing on binding systems from industrial by-products. The use of other underutilized industrial by-products to produce

cementitious binders is of increased interest, since the majority of blast furnace slag and fly ashes have been reserved for use in blended PC [3]. This also provides technological opportunities to make the cement and construction industry more sustainable by utilizing circular economy principles. In our previous works, ladle slag (LS) (i.e., a by-product from steelmaking process) has been effectively used to produce an ettringite-based binder (here abbreviated: LSG) by activating the slag with a gypsum source [8]. To produce the binder, the only pre-treatment needed for raw materials is milling, while citric acid is used to control the workability of the binder. Despite its simple production process, the ettringite-based binder reaches very high compressive strength (70–80 MPa [8,9]) and increased ductility with post-peak hardening behavior when reinforced with polypropylene (PP) fiber [10,11].

Similar to other alternative binders, ettringite-based binders require an understanding of their properties and durability, namely the evolution of mechanical performance during their service life [1,2]. In the literature, the carbonation of ettringite-based binders has been widely reported and discussed [12,13] since ettringite is one of the main hydrates, and the carbonation of this phase can lead to an increase in porosity due to the decomposition of its crystal structure [14].

Ettringite-based binders are also known for their faster rate of carbonation compared to PC [12]. In addition, the crystallization pressure from the formation of ettringite and other hydrates (e.g., strätlingite, calcium aluminate hydrates, and monosulfate) is considered as the main factor influencing the volume stability of these binders [15,16]. Once the crystallization pressure of ettringite creates a stress state exceeding the strength of the binder, cracks can form and propagate leading to expansion and eventually failure [15]. Particularly for unreacted reactants, such as hard-burned MgO in the LSG binder, there is an open question whether these leftover phases will hydrate and generate pressure in the material leading to failure at the macroscopic scale.

There is a lack of published data in terms of potential factors that can lead to the deterioration of alternative cementitious binders. Among those factors, f-MgO (periclase) deserves better attention since CSA cement clinkers often contain 0.8–1.1 wt% periclase [17], whereas this fraction would be much higher if the clinker was sintered from industrial by-products (ca. 4–6 wt% [18,19]). The hydration of f-MgO can lead to the precipitation of $Mg(OH)_2$ (brucite), and this has been reported to cause a 2.2 fold volume increase and an 118% molar volume increase [20,21]. With recent developments in the field of concrete durability [22–25], crystallization pressure, caused by the precipitation and growth of crystals in porous network, can explain more plausibly the crack formation and expansion of the cementitious binders. Therefore, the phase evolution and long-term mechanical performance of these ettringite-based binders are of interest to gain insights into the performance of ettringite-based binders. This is particularly interesting if changes in their microstructure and phase assemblage can be captured by both experiments and thermodynamic modelling.

This study, therefore, aims to investigate the evolution of phase assemblage and the mechanical performance of LSG, as well as the effects of PP fibers on reinforced composite. We investigate the crystallization pressure caused by the precipitation and growth of $Mg(OH)_2$ from a supersaturated solution of Mg^{2+} and OH^- [26] potentially leading to the crack formation and expansion of the binder by thermodynamic modelling and experimentally by phase characterization. The phase evolution of LSG, considering time and curing temperature, is investigated with X-ray diffraction (XRD), using a scanning electron microscope (SEM) coupled with X-ray energy dispersive spectroscopy (EDS). In addition, thermodynamic modelling is adopted to predict the evolution and correlate these changes with the mechanical performance of materials. Regarding the mechanical performance of the materials, variations in their flexural behavior and compressive strength when aged in a water bath at both ambient and elevated temperatures (i.e., 23 °C and 60 °C) are used to investigate mechanical retention properties. Changes in material strength by time can indicate the development and/ or deterioration process caused by potential delayed ettringite formation

and the hydration of f-MgO in the binder, and hence provide essential information for understanding the mechanical behavior of the binder and its composite over their service life.

2. Materials and methods

2.1. Materials

The LS was collected from a slag cooling pit (supplied by SSAB Europe Oy, Finland). The slag was sieved with a 2-mm sieve to remove all the leftover steel flakes prior to milling to reach a d_{50} value of around 10 μm. A synthetic gypsum ($CaSO_4.2H_2O$ supplied by VWR Finland, product code 22451.360) was employed as a calcium sulfate source in this study; the gypsum has a d_{50} of ca. 10 μm. The particle size distributions of LS and gypsum were measured by a laser diffraction technique with a Beckman Coulter 13,320 (Beckman Coulter, the U.S.) in isopropanol. Table 1 shows the chemical compositions and mineralogy of LS and gypsum measured by X-ray fluorescence (XRF) using a PANalytical Omnian Axiosmax at 4 kV and quantitative X-ray diffraction (Q-XRD) using TiO_2 as an internal standard (more details in Section 2.4.2). In addition, EN-196 standard sand was ground to obtain a d_{50} of about 100 μm and used as fine aggregate to produce fiber-reinforced composite from LSG. Regarding reinforcement, high-tenacity PP fiber (Brasilit, Saint Gobain, Brazil) was used to reinforce the LSG binder, and to produce the deflection-hardening ettringite-based composite as reported in previous works [10,11]. Table 2 shows the mechanical and physical properties of the PP fiber. The fiber volume fraction was chosen at 2% to yield the deflection-hardening behavior as optimized in our previous investigation [10].

As for set retarder, citric acid (product code C1949 by Tokyo Chemical Industry Co., Ltd., Japan) was used to control the setting time of mixtures, in which the initial setting time was approximately 1.2 h with 1.8% citric acid solution. To improve the fiber dispersant and flowability of mixtures, a melamine-based superplasticizer (Melment F10 provided by BASF, Germany) and dispersing agent (Darvan 7-N supplied by Vanderbilt, USA) were used. The former was a chemical specified for CSA cements, and the latter was a sodium polymethacrylate based chemical. The dosage of these agents was 0.5% and 1%, respectively, by weight of total binder mass.

2.2. Paste sample preparation

Table 3 shows the mix recipe for LSG in which paste samples (i.e., without sand) were prepared for the phase characterization of the aged binder. A citric acid solution was prepared at room temperature (approximately 23 °C) with a concentration of 1.8% prior to its use. LS

Table 1
Chemical composition and mineralogy (wt%) of raw materials and LSG at initial states measured by XRF and Q-XRD, respectively.

XRF			Q-XRD			
Oxide	LS	Gypsum	Phase	LS	Gypsum	LSG (initial state) [/100 g anhydrous]
CaO	50.6	32.3	Q-phase	47.3	–	4.5
SiO₂	13.9	0.7	C₁₂A₇	21.9	–	1.2
Al₂O₃	24.4	0.1	C₃A	2.4	–	–
Fe₂O₃	0.4	0.1	γ-C₂S	21.0	–	11.7
MgO	3.8	0.4	M	3.9	–	2.8
SO₃	0.4	42.0	Perovskite	2.2	–	1.7
TiO₂	4.1	–	C$\bar{S}$·2H	–	98.2	–
Others	1.4	3.1	C$\bar{S}$	–	1.8	–
LOI (at 950 °C)	1	21.3	Amorphous	1.3	–	41.7
*Monosulfate is often underestimated via XRD due to its low crystallinity.			Ettringite	–	–	21.2
			Monosulfate*	–	–	4.6
			Strätlingite	–	–	0.2
			Katoite	–	–	3.7

Table 2
Mechanical and physical properties of PP fiber.

ID	Type	Young's modulus (GPa)	Elongation at break (%)	Tensile strength (MPa)	Length (mm)	Diameter (μm)	Density (g/cm^3)
PP	Multi-fiber	9	22	910	10	12	0.91

Table 3
Mix proportions (by mass) of the LSG reinforced with PP fiber.

Sample ID	Slag (g)	Gypsum (g)	Sand (g)	Citric acid[a]	W/B[b]	PP fiber volume fraction
LSG PP-LSG	70	30	50	1.8 wt%	0.45	– 2%

[a] Citric acid mixed with water to produce a solution with 1.8 wt% concentration.
[b] W/B (water-to-binder ratio) with total binder mass calculated as the sum of the masses of slag and gypsum.

and gypsum were dry-mixed together prior to mixing with the citric acid solution by a shear mixer. The paste was cast into cylindrical molds with a diameter of 25 mm and height of 20 mm. Samples were cured at room temperature for 24 h in closed plastic bags, and then demolded and cured in water for 27 days prior to curing at elevated temperature of 60 °C.

2.3. Fiber reinforced mortar preparation

The mix proportions of LSG and its PP fiber reinforced composite (PP-LSG) are shown in Table 3. Powdered materials including LS, gypsum, fine sand, and the superplasticizer were weighed and dry-mixed in a 5-liter Kenwood mixer at low and high speed (70 rpm and 150 rpm, respectively) for 1 min at each level. The dispersing agent was mixed with a citric acid solution and added gradually to the powdered mixture. The mortar was mixed at the low speed for 3 min. The fibers were added gradually to the mortar while using the low mixing speed. When all fibers were added to the mortar, mixing was continued for 10 min at high speed. The whole mixing sequence took ca. 20–25 min. Mortar samples were cast into oiled molds, vibrated for 3 min at a frequency of 1 Hz, and cured at room temperature for 24 h in closed plastic bags. After demolding, samples were cured in water for 27 days and then dried in laboratory conditions (room temperature and RH% = 40–50%) for 7 days prior to further aging and characterization.

2.4. Experimental features and procedures

2.4.1. Material aging at hydrothermal condition

Specimens were fully immersed in a thermostatic water bath (model JB2, Grant Instruments Ltd., England) using deionized water for 1, 2, and 4 months at 60 °C, with samples cured at 23 °C considered as reference material. The thermostatic bath contained 12 l of water with a temperature range of 20–120 °C and a tolerance of ±1 °C. The bath was constantly covered with a polypropylene foil to minimize evaporation of the water. This curing temperature and water-saturated condition were selected based on a relevant study by Kaufmann et al. [27] on CSA cement at elevated temperature. The authors reported the decomposition of ettringite at 90 °C, while strätlingite converted to siliceous hydrogarnet (Si-hydrogarnet) at 70 °C based on thermodynamic modelling [27]. Jeong et al. [28] also found the decomposition and reformation of ettringite plays a key role in the strength development of the binder, depending on the mineralogy of CSA clinkers, the presence of sulfate, and elevated temperatures. Therefore, to prevent the decomposition of hydrates in LSG and to capture the phase evolution caused by further reaction of the precursors, the maximum aging temperature was set to 60 °C. This temperature should capture the most prominent changes in the phase evolution of the binder in accelerated aging

conditions without altering the entire phase assemblage [29].

2.4.2. Phase characterization

XRD and SEM/EDS were selected to characterize the changes in the mineralogy of the LSG paste, phase assemblage, and morphology, cured in water at 60 °C. XRD analysis was performed on powdered samples using a Rigaku SmartLab 9 kW employing Co-Kα radiation (Kα1 = 1.78892 Å; Kα2 = 1.79278 Å; Kα1/Kα2 = 0.5). The measurements were conducted at a scan rate of 3°/min in the range 5°–90° (2θ) and 0.02°/step. Q-XRD analysis was used to determine the fraction of amorphous phases in LSG using TiO$_2$ (measured values roughly 10 wt%) as an internal standard. Phase identification was done using PDXL V.2 software (Rigaku, Japan) and a PDF-4+ 2020 database.

The microstructure of LSG at different aging times (i.e., 1, 2, and 4 months of aging) was investigated through SEM using a Zeiss Ultra Plus (Germany) with a 15 kV accelerator voltage and a working distance of 7–8.5 mm. Prior to the phase characterization, the hydration of the samples was stopped by solvent exchange using isopropanol. The SEM samples were vacuum-impregnated with low-viscosity epoxy resin. After the hardening of the resin at room temperature, samples were polished with diamond discs in a range of 220–1 μm at 150 rpm using ethanol as lubricant. The pastes were coated with carbon and observed using backscattered electrons (BSE). The chemical compositions were measured using an X-Max EDS detector (by Oxford Instrument, the UK). To further investigate the effects of late reaction products on the microstructure of the binder, an EDS hypermap was acquired using Oxford Instrument Aztec software (the UK) with a resolution of 1024 × 768 pixels and a dwell time of 200 μs for a total 10 frames. The hypermap was quantified using the QuantMap function in the Aztec software for all elements without any normalization. The segmentation and analysis of the EDS hypermap were done using the *edxia* method [30] in *Glue*'s interface [31] with the input of a BSE image and all elements as text files.

2.4.3. Thermodynamic modelling

Thermodynamic calculations were based on the Gibbs free energy minimization method where GEMS software, developed by the Paul Scherrer Institute (Switzerland) [32,33], was used for the modelling. GEMS is a geochemical modelling code that is employed to compute equilibrium phase assemblage and speciation in complex chemical systems. In this study, the Cemdata18 database [34], which is a dedicated database for cementitious systems, was used together with a thermodynamic default database embedded in GEMS [33]. These databases contain the solubility constants of the hydrated solids in the most common cementitious binders, such as AFt (including ettringite), AFm (including monosulfate) phases, hydrogarnet, and hydrotalcite [34].

The modelling considered the hydration kinetics of phases in LS, namely the Q-phase (i.e., a quaternary phase $C_{20}A_{13}M_3S_3$), mayenite ($C_{12}A_7$), gamma belite (γ-C_2S), and tricalcium aluminate (C_3A). Periclase (MgO, approximately 2–3 wt% in the slag) is a hard-burned phase, therefore only dissolved at elevated temperature, while karooite and perovskite were seen as inert in the slag. This study used an empirical kinetic equation, proposed in Ref. [35] as shown in Eq. (1), to implement the hydration kinetics of the individual phases of LS and gypsum. The input for the equation was from experimental results which determined degrees of hydration as a function of time for each individual phase. The empirical kinetic equation is

$$\mathbf{Q_i(t) = Q_{i0} + k_i e}^{\left(-n_i/t\right)}, \tag{1}$$

where: i indicates different anhydrous phases in the mixture; $Q_i(t)$ is the dissolved mass of an individual anhydrous phase at a time t; Q_{i0} is a constant that indicates the initially fast dissolution/hydration of a phase; k_i is a limitation of a phase's availability for hydration during the period of investigation; and n_i is a parameter indicating the rate of hydration of the phase. To allow for the direct calculation in GEMS, the exponent of the exponential function needs to be in the interval $-70 \leq x \leq 70$, which may restrict the hydration times investigated. If necessary, the function can be solved using different software and then implemented as a column of hydration factors ($0 \leq f(x) \leq 1$) into GEMS.

The saturation index (SI) of different precipitates were calculated based on Eq. (2),

$$\mathbf{SI} = log \frac{\mathbf{IAP}}{\mathbf{K_{so}}} \tag{2}$$

where: IAP is the ion activity product using the input from the thermodynamic calculation limited by the degree of hydration in LS and gypsum; and K_{so} is the theoretical solubility of the precipitates. An upper threshold of phase precipitation for the critical phases (e.g., brucite) was chosen based on the initial hydration condition to be able to calculate the SI in Eq. (2); in the GEMS model, the *dul* threshold was set to 0.01 M, which is slightly higher than the initial mol quantity of OH-hydrotalcite in the system ($X_a = 0.007$ M).

The maximal crystallization pressure generated by precipitates in a supersaturated solution is calculated using Eq. (3) [23],

$$\mathbf{\sigma} = \frac{\mathbf{R_g T}}{\mathbf{\upsilon_{crystal}}} ln \left[\frac{\mathbf{IAP}}{\mathbf{K_{so}}} \right] \tag{3}$$

where: R_g is the gas constant; T is the absolute temperature (K); $\upsilon_{crystal}$ is the molar volume of precipitates; and $ln(IAP/K_{so})$ is taken from Eq. (2). Note that the crystallization pressure reported in this work represents the worst-case scenario that might occur in the binder. Otherwise, the actual crystallization pressure depends on the surface energy of the different crystal orientations and is often idealized as curvature of the surface of the growing crystals in the models used for explanation of the mechanism.

2.4.4. Mechanical testing

The mechanical performance (i.e., flexural behavior and compressive strength) of the plain LSG and PP-LSG were considered after each aging period and temperature (23 °C and 60 °C). After 1, 2, and 4 months of aging, specimens were subjected to 4-point bending and compressive tests using a Zwick device (Germany) with a load cell of 10 and 100 kN, respectively. Moreover, to capture the rate of phase evolution and corresponding mechanical changes between ambient and elevated temperature, the mechanical performance of materials aged at 40 °C for 4 months was tested to provide additional information. Fig. 1 shows the setup for the bending test, and the geometry of the specimen. Three specimens for each composition, temperature, and aging period were tested to determine the flexural and compressive characteristics of the LSG and PP-LSG. Displacement control was used in the bending and compressive test with a speed rate of 0.4 and 1 mm/min, respectively. The flexural strength and stiffness were calculated according to ISO and

ASTM standards [36,37], respectively, using

$$\mathbf{\sigma_f} = \frac{\mathbf{FL}}{\mathbf{bh^2}} \tag{4}$$

$$\mathbf{E_f} = \frac{\mathbf{0.21 L^3}}{\mathbf{bh^3}} \left(\frac{\mathbf{\Delta F}}{\mathbf{\Delta s}} \right) \tag{5}$$

where: σ_f and E_f refers to flexural strength and stiffness, respectively; F is maximum load; L is span; b and h are width and high of the specimen, respectively; and ΔF and Δs are the difference in load at two corresponding midspan deflection points of the initial linear portion of the load-deflection curve. The compressive strength was measured by loading halves of the prismatic bending specimens and calculated according to EN 196-1 [38].

During the bending test, the 2D digital image correlation (DIC) technique was utilized to monitor the crack pattern evolution of the samples. Images were captured using a camera with a shooting frequency, aperture, and shutter speed of 1 Hz, f/4.0, and 2000 μs, respectively. LaVision StrainMaster [39] software was used to analyze images at the area of interest (AOI) as indicated in Fig. 1. Parameters for correlation were subset size 37 and step size 3. Data from the postprocessing of images provided the information regarding crack patterns as well as the measurement of crack opening displacement (COD) for all cracks from the full field observation of DIC. Samples for the bending test with DIC analysis were prepared with a white-painted surface and randomly-distributed black acrylic paint dots.

3. Results and discussions

3.1. Phase assemblage and evolution

Ettringite was stable in the binder during the aging period, while there were some changes in the phase assemblage of LSG at elevated temperatures. Fig. 2 shows the XRD diffractograms of LSG after 1, 2, and
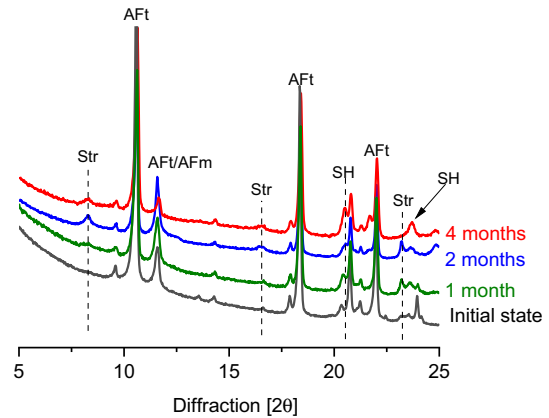
Fig. 2. XRD diffractograms of LSG paste after 1, 2, and 4 months of aging at 60 °C (Str: strätlingite, SH: Si-hydrogarnet, AFt: ettringite, and AFm: monosulfate).
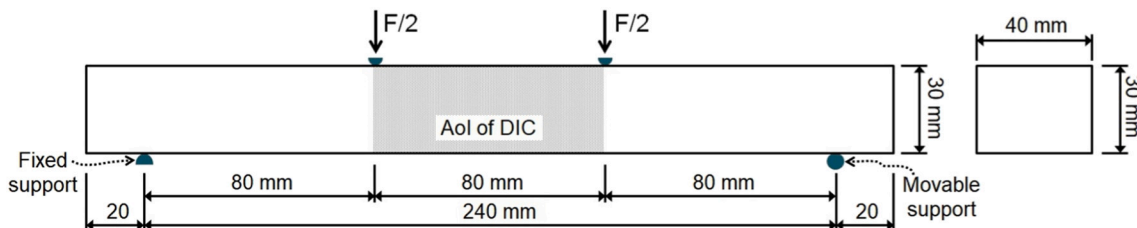
Fig. 1. Scheme of the 4-point bending test for specimens in which the area of interest for the digital image correlation is marked in gray.

4 months aging in water at 60 °C in comparison to the initial stage of the binder. Ettringite is the main crystalline phase in the binder, which occupied roughly 25 wt% of the paste sample. There was no change in the stability of this crystal at 60 °C in the water-saturated condition since ettringite will only start its decomposition to gypsum and monosulfate at 90 °C based on thermodynamic calculations [27]. Strätlingite was found in all the aged samples, in which its presence was clearly seen after 2 months (ca. 9 wt%). This hydrate was also found in the sample aged at the ambient temperature after 9 months (Fig. A1 of the Appendix). At later stages, Si-hydrogarnet was also observed. A trace of Si-hydrogarnet (ca. 4 wt%) was found in the LSG paste at the initial stage, and after the 4th month of aging this hydrogrossular phase was around 10 wt% in the binder. In Ref. [27], strätlingite was thermodynamically calculated to be unstable compared to Si-hydrogarnet at around 70 °C. Based on the Q-XRD result, the amount of strätlingite was approximately 5 wt% after the aging period. Note that there was an amorphous fraction (ca. 25 wt%) in the aged binder, which is attributed to a C–(A–)S–H and aluminum hydroxide gel, and low-crystalline monosulfate.

Fig. 3 shows the degree of hydration of individual phases in LS (i.e., $C_{12}A_7$, Q-phase, γ-C_2S, and MgO) and gypsum, obtained from Q-XRD analysis. Note that there was a small amount of C_3A (ca. 2 wt%) in the slag, but this completely reacted after 7 days as also reported in our previous study [8]. LS continued its hydration at the elevated temperature and water-saturated storage condition. After 4 months of aging, $C_{12}A_7$ and Q-phase had completely reacted, while γ-C_2S reached a degree of hydration of approximately 90%. The dissolution of these phases provided more Ca, Al, Mg, and Si into the system, which in turn precipitated more monosulfate, C–(A–)S–H gel, strätlingite, and Si-hydrogarnet in the binder. In addition, there was roughly 3 wt% of hard-burned MgO in the LS, which is also often present in the CSA clinker and was reported to have low reactivity [19,40]. However, in this study, brucite [Mg(OH)$_2$] formed in the aged samples after 2 months. Notably, a part of Mg in the system originated from the Q-phase (i.e., $C_{20}A_{13}M_3S_3$).

The microstructure of the aged samples shows that the precipitation and growth of brucite can lead to potential stress in the binder (Fig. 4). The microstructure remained stable and sound after 1 month of aging compared to the initial stage. Ettringite, monosulfate, and C–(A–)S–H phase were present in the microstructure, while MgO was unreacted (Fig. 4a). However, from the 2nd month onward, hard-burned MgO started to react forming a rim of brucite surrounding MgO particles (Fig. 4b) and eventually the precipitation of brucite as seen in Fig. 4c. This deleterious expansion caused micro cracks in the structure as observed from the EDS mapping of Mg in Fig. 5. Cracks were generated due to the pressure from crystallization in pores and interconnected Mg-rich areas (i.e., brucite). These damages in the microstructure led to diffuse macro cracks in the plain LSG and resulted in the reduction of its mechanical performance which is detailed in Section 3.2. Notably, the elevated temperature affects the hydration kinetics of f-MgO, in which it took only 2 months to form a brucite rim surrounding MgO particles in the LSG sample at 60 °C, but double time at 40 °C (Fig. A2).

The EDS analyses show an intermixed C–(A–)S–H gel and a high level of Mg-blended phases in the binder after aging periods (Fig. 6). At the initial stage, the C–(A–)S–H gel was rich in Al and Ca, whereas the compositions shifted toward Si-rich gel with the formation of strätlingite and Si-hydrogarnet after the aging time (Fig. 6a). This was due to the dissolution of γ-C_2S that provided significantly more Si into the system, while there was also an increase in the amount of Ca and Al from the dissolution of $C_{12}A_7$ and Q-phase. Notably, γ-C_2S is known to display a low dissolution rate due to its olivine structure [41]. However, the dissolution and degree of hydration of this phase increased significantly under elevated temperatures and water-saturated aging conditions. The aged samples had higher Mg-blended areas (Fig. 6b) that indicate an increase in the fraction of Mg-bearing phases (e.g., hydrotalcite and brucite) in the binder. Furthermore, the atomic composition of aged pastes leaned toward the Mg(OH)$_2$ and MgO composition (i.e., on top of the Mg axis) indicating the presence of these phases in the microstructure.
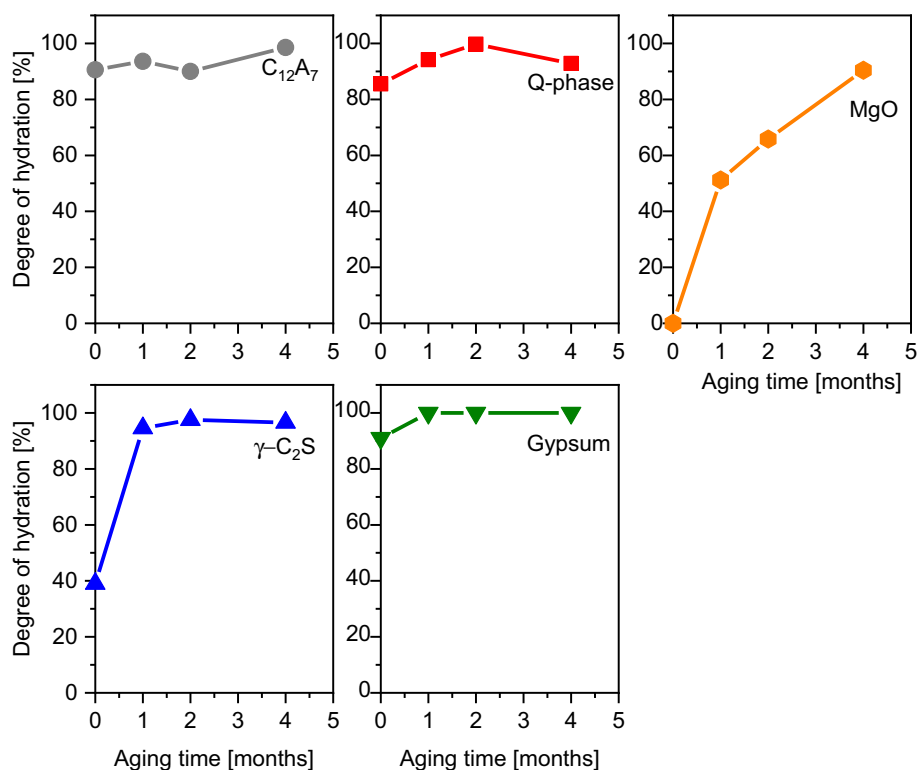

Fig. 3. Degrees of hydration (%) for individual phases in paste samples of LSG aged at 60 °C (the initial stage is represented as the 1st month) determined from Q-XRD results (estimated error 5%). Note that C_3A completely reacted after 7 days of hydration and MgO was unreacted prior to the aging.
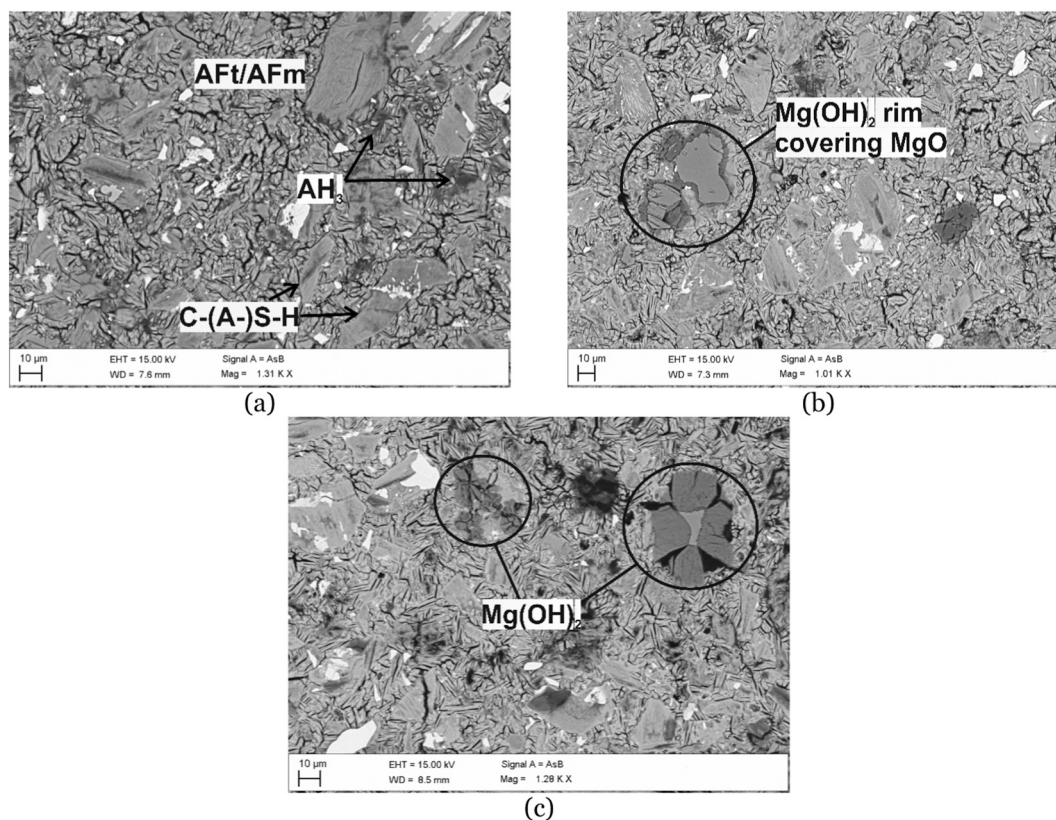
Fig. 4. Microstructure of LSG paste after (a) 1, (b) 2, and (c) 4 months of aging at 60 °C analyzed by SEM/EDS.

The degree of hydration of phases in LS and gypsum (in Fig. 3) was used to implement the hydration kinetics for a thermodynamic model. By considering the hydration kinetics in the modelling, it is possible to capture phase evolution as well as volume changes in the binder under the aging scheme. In contrast, a model built without kinetic input overlooked the changes in phase assemblage and led to a difference of ca. 15% in the amount of precipitates when compared with the experimental data from the Q-XRD analysis. Table 4 shows the input parameters used in Eq. (1) to represent the hydration kinetics of individual phases in LS and gypsum.

Since the initial stage of LSG is the sample at 28 days, the majority of Q-phase, $C_{12}A_7$, and gypsum have reacted (see Fig. 3). Therefore, the Q_0 value of these phases were set to 75, 80, and 85, respectively. In contrast, γ-C_2S had poor reactivity [42] leading to a low degree of hydration after 28 days of curing ($Q_0 = 20$), while the hard-burned MgO was unreacted ($Q_0 = 0$) at ambient conditions. Under the aging scheme, the phases in LS continued their reaction at different rates. The Al-containing phases (i.e., Q-phase and $C_{12}A_7$) dissolved completely, where $C_{12}A_7$ exhibited faster dissolution ($n = 10$) than that of Q-phase ($n = 30$). There was a trace of these phases (ca. 0.5–1 wt%) left in the binder after the aging time; however, the fraction was minor and within the measurement error of the XRD technique. Note that $C_{12}A_7$ is known as a highly reactive phase, which can accelerate the hydration in ettringite-based binders [8,43], hence $C_{12}A_7$ often reached a degree of hydration over 80% after 28 days. Gamma-C_2S attained higher reactivity with the degree of hydration reaching 80% when aged at the elevated temperature; this is the major source of Si in the system other than a minor amount of Si coming from the Q-phase. Importantly, the hard-burned MgO turned out to be reactive and was assumed to completely react in a long term.

The thermodynamic modelling indicated the phase evolution of LSG when the leftover precursors continue their hydration at 60 °C (Fig. 7). Significant change was observed after 2 months of aging when ettringite

slightly dissolved to form more monosulfate, while aluminum hydroxide reacted completely to form strätlingite. The formation of C–S–H gel was found in a small fraction starting after 4 months of aging. The thermodynamic model predicted OH-hydrotalcite as an Mg-bearing phase while brucite was experimentally found in XRD and SEM. In contrast, OH-hydrotalcite formed in a small fraction surrounding Q-phase grains as reported in our previous work [44]. Furthermore, the EDS hypermap in Fig. 5 indicated the formation of intermixed brucite with a minor amount of Al. This may be explained by the delayed hydration of MgO, whereas OH-hydrotalcite was observed in relation with the Q-phase but may form from brucite over much longer curing times. Hence, both phases were allowed in the thermodynamic modelling. Note that there was a gradual increase in the total volume of the system due to the precipitation of hydrates in the binder (e.g., brucite, strätlingite, and monosulfate). However, deterioration as observed in the binder should not be explained by volume increase alone, but rather originating from the crystallization pressure from crystals formed in supersaturated pore solution [25].

The crystallization pressure generated by the precipitation of brucite is in-line with the deterioration in the aged LSG and is therefore a more plausible explanation for the observed damages. Fig. 8 shows the SI of brucite and OH-hydrotalcite, and the crystallization stress generated during their precipitation. After 1 month of aging at 60 °C, brucite was undersaturated and did not precipitate in the binder. Hence, the crystal did not produce any pressure on the matrix, which was still sound as seen in Fig. 4a. From the 2nd and 4th months, brucite reached saturated and oversaturated conditions, respectively, that generated up to ca. 200 MPa of pressure on its surroundings and eventually caused the formation of cracks in the microstructure (Fig. 5). Similar deterioration caused by f-MgO hydration was reported in Ref. [29] under a similar aging scheme for a PC concrete sample in water and at an elevated temperature. Thermodynamic modelling suggests that the pore solution is also supersaturated with respect to OH-hydrotalcite, which could also

(a)

(b)

(c)
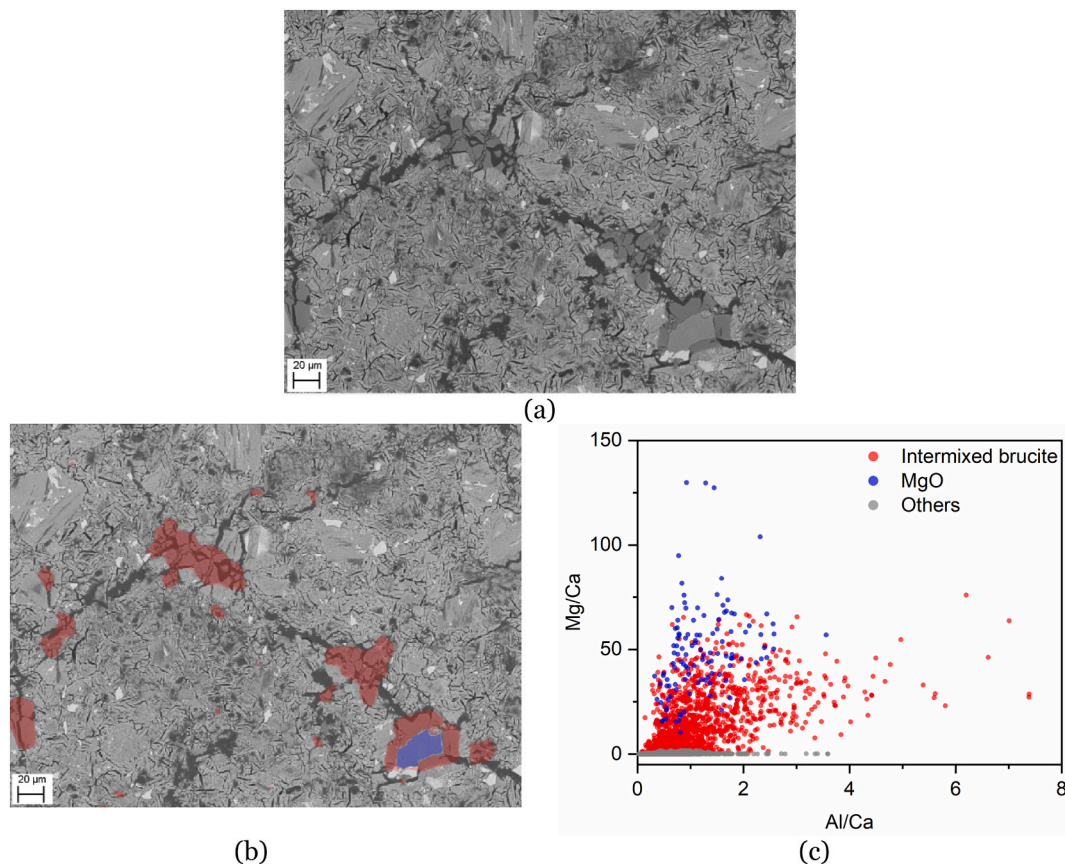
Fig. 5. (a) A backscattered SEM image and (b) segmented image for the EDS hypermap of LSG paste aged at 60 °C after 4 months, in which the segmentation was based on (c) the atomic ratios of Mg in the system. Red and blue areas represent Mg-bearing phases, for which their precipitation generated interconnecting cracks in the binder. (For interpretation of the references to colour in this figure legend, the reader is referred to the web version of this article.)

contribute a significant expansive force on the binder after 2 months of aging. However, the electron microscope observations suggested that MgO hydrated before it may be mixed with hydrotalcite. The calculation of SI and the related maximum crystallization pressure have been possible due to the limitation of brucite and hydrotalcite precipitation ca. 40% above the small initial estimated hydrotalcite quantity. Brucite and OH-hydrotalcite co-exist in the binder after MgO has hydrated, which was observed experimentally.

3.2. Mechanical performance

This Section discusses the evolution of the mechanical performance of the fiber reinforced LSG in comparison with the plain material in different aging temperatures. The discussion focuses mainly on 2 aspects:

- the deterioration of the binder at elevated temperatures linked to the late hydration of MgO in phase assemblage, as discussed in Section 3.1, and
- the role of PP fiber in improving the durability and mechanical performance of the developed composite.

3.2.1. Sample appearance

Both plain and reinforced LSG were sound, by visual observation, after 2 months of aging at an elevated temperature, while the macroscopic deterioration was observed clearly after the 4th month. Fig. 9 shows the appearance of both compositions aged in water at 60 °C for different periods. Note that the samples aged at an ambient temperature did not show any cracks on both plain and fiber reinforced LSG, while

the plain sample aged at 40 °C formed micro cracks after 4 months as shown in Fig. A3 of the Appendix. The formation of cracks is in-line with the precipitation of brucite in the binder due to the reaction of the hard-burned MgO at the elevated temperature. As observed via XRD and SEM/EDS, brucite started forming (i.e., a rim covering MgO particles) after 2 months and exerted expansive forces leading to the formation of micro cracks after 4 months. This transpired at the macro scale of samples where cracks started propagating in the plain LSG after the same aging period. PP fiber effectively reduced damage evolution from the crystallization pressure via its fiber bridging effect that delayed crack propagation [45]. Some cracks appeared on PP-LSG after 4 months (Fig. 9), but their number, width, and extension were much less than those of the plain LSG (see Fig. A4). Notably, the higher aging temperature led to larger crack width in the plain LSG, whereas this difference was much less obvious in the PP-LSG.

3.2.2. Flexural behavior

Fig. 10a shows the evolution of flexural strength of LSG and PP-LSG at different aging times and temperatures. There was a slight increase in the strength of plain LSG after the 1st month aged at room temperature; this is likely due to further reaction between LS and gypsum leading to a denser matrix as well as a better bonding between fiber and matrix in the case of PP-LSG. The reduction in flexural strength of LSG was clearly seen after the 4th month, which is in-line with the observation of the sample appearance and microstructure. After 4 months in water at 40 and 60 °C, the flexural strength of LSG decreased by approximately 30% and 45%, respectively, in comparison to its initial stage. In contrast, there was negligible reduction in the plain sample aged at ambient conditions. Therefore, this ettringite-based binder ages well at the ambient temperature and yet is expected to suffer from the degradation
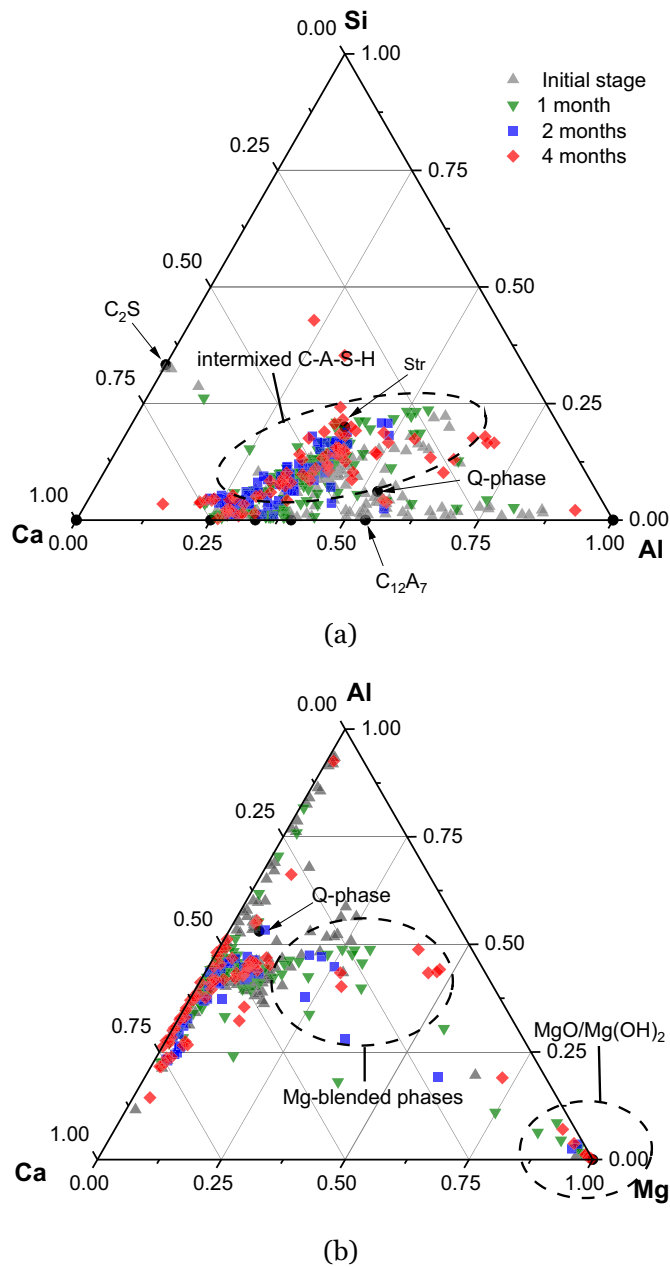
(a)

(b)

Fig. 6. Atomic plots obtained from SEM/EDS for the ternary plot of (a) Ca-Al-Si and (b) Ca-Al-Mg system where black dots represent the theoretical atomic ratios of the phases indicated.

Table 4
Parameters used in Eq. 1 for modelling the hydration kinetics of phases in LS and gypsum in LSG aged at 60 °C.

Phase	Q_0	n	k
Q-phase	75	30	25
$C_{12}A_7$	80	10	15
γ-C_2S	20	20	80
Gypsum	85	20	15
MgO	0	25	100

of its mechanical performance at elevated temperatures due to the re-action of hard-burned MgO as aforementioned.

PP fiber significantly improved the flexural strength and retained composite strength when compared with the plain LSG. As for the unaged samples, the average flexural strength of PP-LSG attained 10
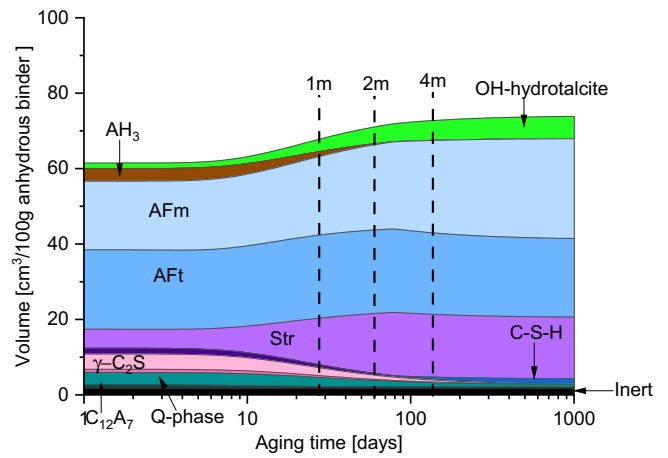
Fig. 7. Thermodynamic modelling for the phase evolution of LSG aged at 60 °C.

MPa, which was 60% higher than that of the unreinforced material (Fig. 10a). The reduction rate of the composite was also lower than that of the plain LSG. After 4 months in water at 40 and 60 °C, the average flexural strength of PP-LSG was almost unchanged and 80%, respectively, compared to unaged samples. Compared with the unreinforced LSG after 4 months at 60 °C, the average flexural strength of PP-LSG (i.e., 8 MPa) was ca. 2 times higher. Hence, PP fiber plays an important role in delaying crack propagation caused by internal stress [45] from crystallization pressure and eventually slows down the degradation process. In addition, it is worth noting that the incorporation of PP fibers increased the total percolated pore volume of the composite (see Fig. A5), which could contribute to increased energy absorption from crystallization stress.

In both LSG and PP-LSG, the decrease in the flexural modulus of elasticity was clearly seen in the samples aged at 60 °C (Fig. 10b). Although the modulus at the initial stage was similar for both materials, PP-LSG exhibited a slower rate of degradation. The plain material dropped its elastic modulus under flexural load by 64% after 4 months, while that of PP-LSG was roughly 50% in the same period. This can be attributed to the contribution of PP fiber to the matrix via the fiber bridging action that transferred the loads caused by the crystallization pressure from brucite formation. As reported in other works [45–47], fibrous reinforcement is known to reduce the risk of expansion from physical (e.g., freeze-thaw attack) or chemical (i.e., sulfate attack) loads—or from these combined loads. Note that the degradation process in LSG and PP-LSG had already initiated after the first month of aging at 60 °C. In contrast, the flexural modulus of plain and reinforced LSG aged at 23 °C and 40 °C remained unchanged after 4 months of aging. Notably, the flexural modulus of elasticity of LSG at ambient temperature increased by roughly 80% in the first 2 months of aging. This may be due to some further reactions from Al-containing phases in LSG leading to a more compact matrix.

The PP-LSG attained deflection-hardening behavior under 4-point bending tests regardless of aging period and conditions. Fig. 11 shows the average (calculated from triplicate tests) stress vs. COD (i.e., calculated from DIC) curves of the reinforced material divided into three blocks according to the aging temperature. It is worth mentioning that all the unreinforced materials exhibited brittle behavior with a COD at failure of less than 0.05 mm. Therefore, the data of plain LSG was left out in Fig. 11 for better comparison of reinforced LSG in different aging conditions. The initial crack of PP-LSG appeared under bending load in the range 5 to 7 MPa for aged samples. After the onset of the initial crack, the PP fiber started its bridging action, which transferred the load between fibers and matrix and eventually led to the formation of other cracks in different flaw positions [48]. This mechanism accounts for the hardening behavior of PP-LSG, in which the COD at peak load could
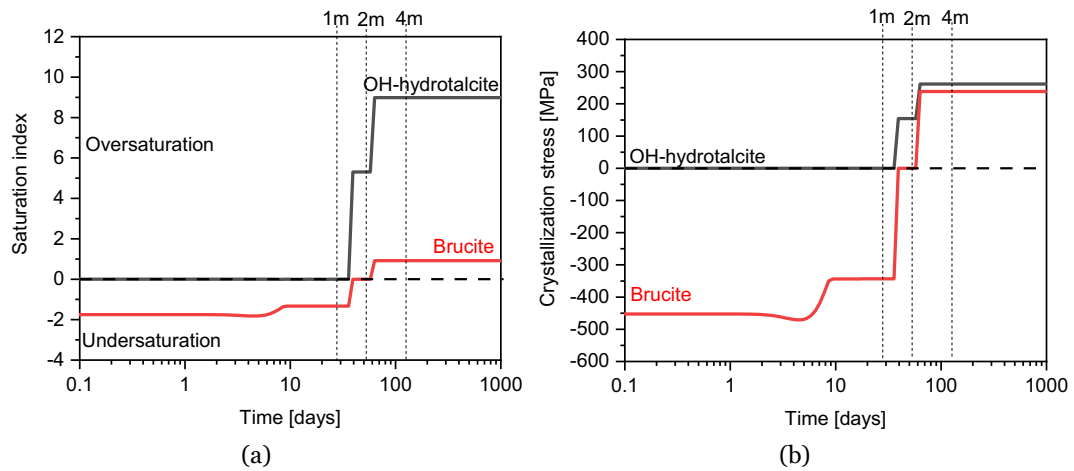
Fig. 8. (a) The saturation index and (b) the crystallization stress of brucite and OH-hydrotalcite calculated from the thermodynamic model with input from the hydration kinetics of LS and gypsum.
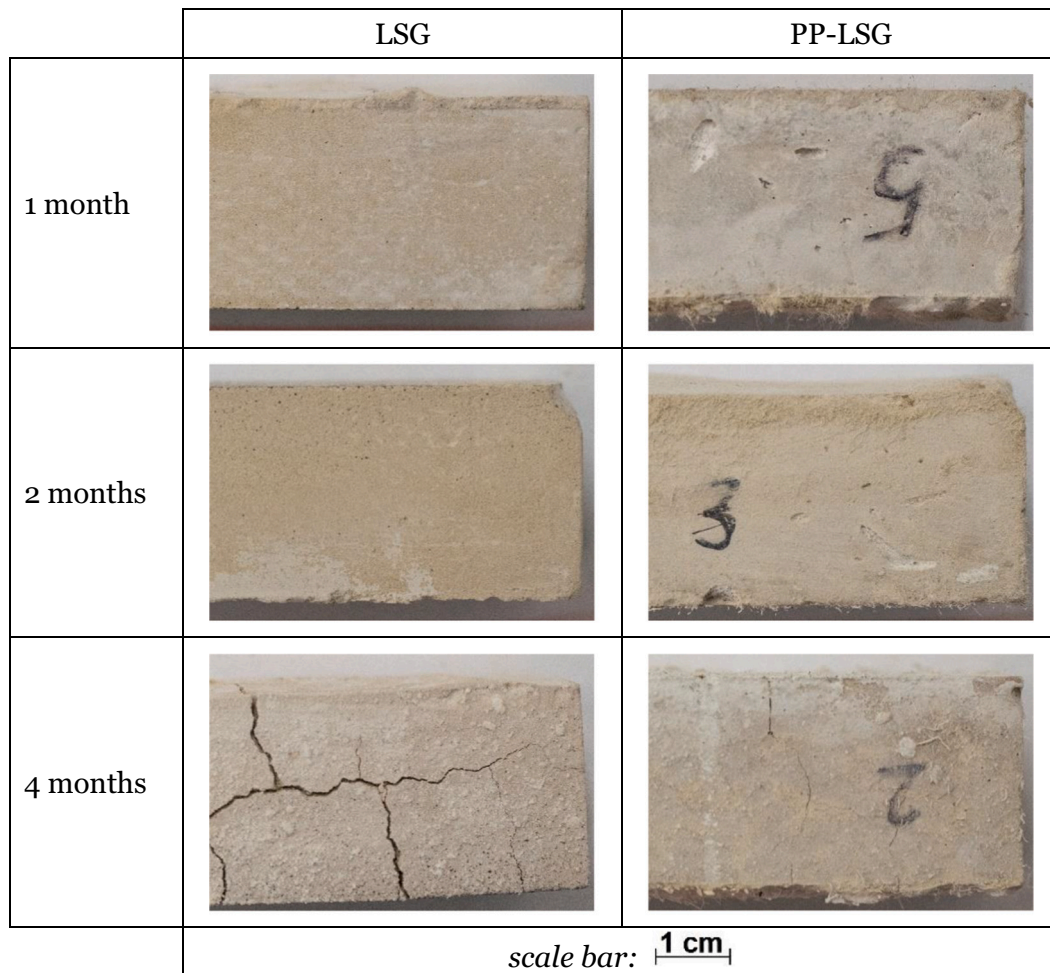

Fig. 9. Sample appearance of LSG and PP-LSG after 1, 2, and 4 months aging at 60 °C in water.

reach approximately 1 mm (i.e., 20 times higher than that of the plain LSG).

The reduction in flexural performance of PP-LSG was clearly seen at 60 °C, while there was no significant decrease observed at other temperatures (Fig. 11). At 60 °C, the composite attained the deflection-hardening behavior with a COD at peak load of roughly 1 mm after the 1st month. In contrast, at the same COD, the composite exhibited softening behavior after the 2nd and 4th month of aging with a stress of ca. 7.1 MPa. Note that the onset crack in samples aged for 4 months at 60 °C was captured by DIC at around 4 MPa (i.e., 40% lower than samples aged for 1 month), which indicated severe damage caused by cracking from hydration of the hard-burned MgO on the LSG matrix at a
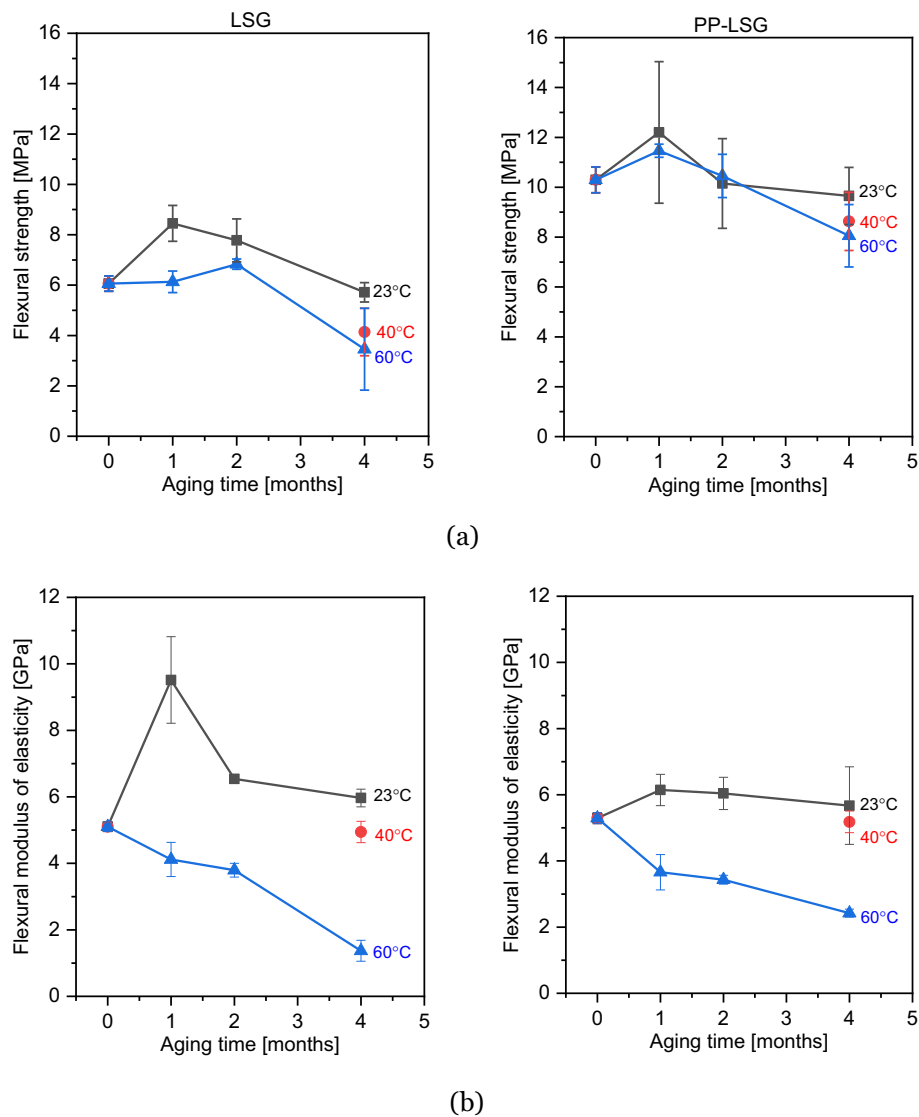
Fig. 10. (a) Flexural strength and (b) flexural modulus of elasticity after different aging periods and temperatures of LSG (left) and PP-LSG (right).

longer aging time. Interestingly, the flexural performance of PP-LSG samples aged at 23 and 40 °C seemed unchanged regardless of aging time (Fig. 11a and b).

3.2.3. Compressive strength

A clear degradation in compressive strength was observed in the plain LSG aged at elevated temperatures, while the reinforced material exhibited a slight reduction (Fig. 12). The unreinforced material encountered a decrease by ca. 30 and 70% in the compressive strength after 4 months of aging at 40 and 60 °C, respectively. In contrast, the PP-LSG reduced only 25% and 40% of its initial strength, respectively. Notably, the PP fiber increased the compressive strength of the reinforced LSG by roughly 25% due to the contribution of the fiber in delaying crack propagation and localization [49], and eventually the driving force for the formation of cracks under compression is curtailed [50]. Therefore, although the damages caused on the matrix are severe, the reinforced LSG still retained a compressive strength of higher than 30 MPa across all aging conditions. Therefore, to meet requirements in construction design codes (e.g., Euro code 2 [51]), the long-term mechanical performance of this binder needs taken into consideration regarding the formation of hydrates that can potentially cause damages in the material.

The compressive strength of both LSG and PP-LSG aged at ambient temperature remained unchanged after 4 months of aging. In addition, the compressive strength of LSG at 23 °C slightly increased after 1 month, which was in-line with the flexural properties shown in Fig. 10. This can be attributed to a development in the LSG matrix due to further reactions in the binder. A similar explanation can be applied for the samples aged at 60 °C after 1 and 2 months. However, the crystallization pressure plays a key role in this case. The crystallization pressure, developing from the saturated pore solution, becomes deleterious in a confined matrix, and eventually causes damage in the material at both the micro and macro scale (Fig. 12).

4. Conclusions

This study investigates the phase evolution and corresponding mechanical performance of an ettringite-based binder under hydrothermal conditions. The investigation provides an improved understanding of further reactions in the binder that can generate deleterious crystallization pressures, particularly resulting from the hydration of f-MgO leading to the precipitation and growth of $Mg(OH)_2$. The PP fibers play an important role in absorbing energy caused by crystallization pressure, and hence increase the strength retention of the fiber-reinforced composite.

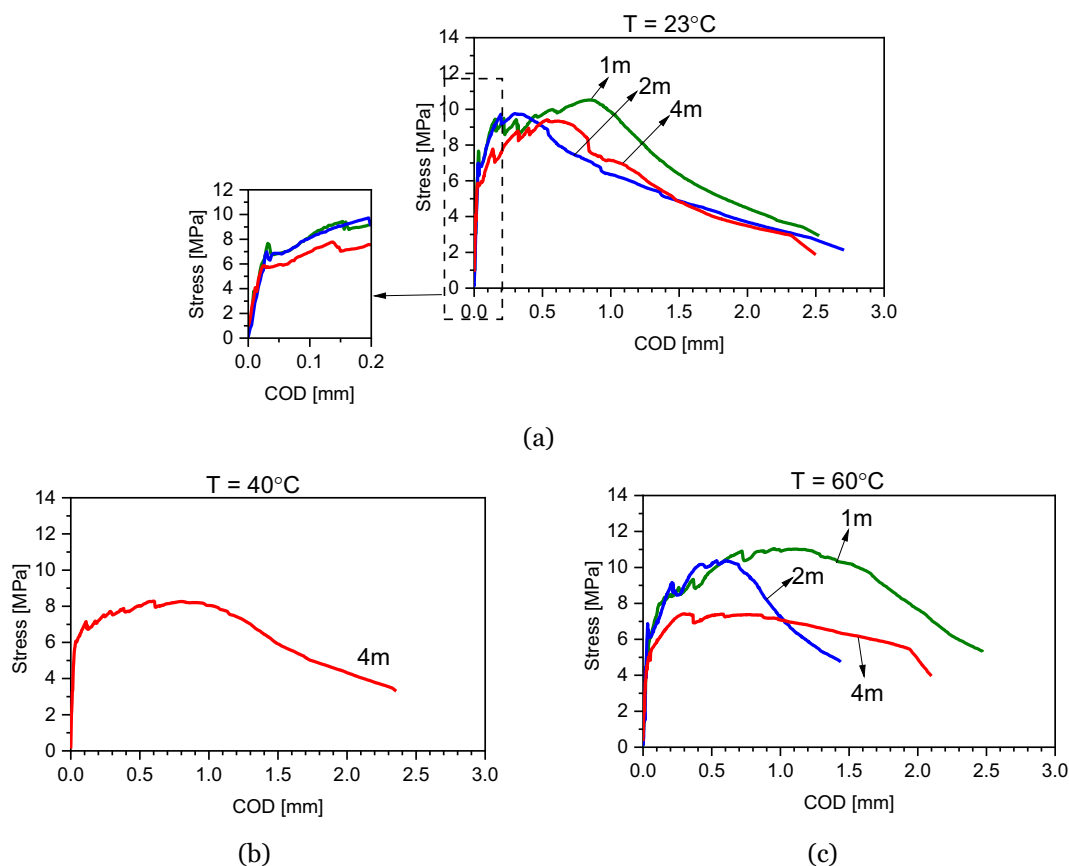Periclase reacts quickly at elevated temperatures (i.e., 60 °C) and

Fig. 11. Flexural tests: average stress vs. COD curves of PP-LSG at (a) 23°, (b) 40°, and (c) 60 °C after 1, 2, and 4 months of aging.
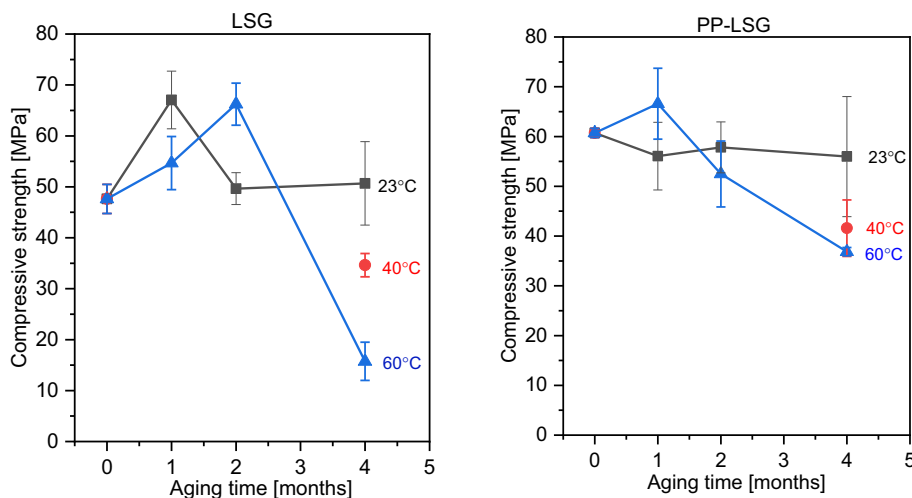

Fig. 12. Compressive strength after different aging periods and temperature of LSG (left) and PP-LSG (right).

reaches a degree of reaction of ca. 90% after 4 months. This leads to the formation of brucite and can generate a crystallization pressure of maximal 200 MPa as estimated by thermodynamic modelling. Microstructural observations in the binder show the formation of microcracks interconnecting among brucite's positions leading to failure at macro scale after 4 months of aging. In contrast, periclase remains unreacted at an ambient temperature, therefore the binder was sound during the aging periods. Ettringite was stable in the binder during the aging period at 60 °C in a water-saturated condition. Si-hydrogarnet was observed after 4 months of aging (ca. 10 wt%) and co-existed with strätlingite.

PP fiber contributes to the strength retention of the fiber-reinforced composite via the ability to delay crack propagation caused by crystallization pressure. In addition, the fiber significantly improves the flexural performance of the composite with deflection-hardening behavior in all aging periods. The compressive strength of the reinforced composition retained 60% of its initial strength. In contrast, the plain material exhibited brittle behavior under bending tests, and the strength retention after 4 months of aging was ca. 30% of its initial compressive strength.

CRediT authorship contribution statement

Hoang Nguyen: Conceptualization, Data curation, Formal analysis, Investigation, Methodology, Validation, Visualization, Writing – original draft, Writing – review & editing. **Valter Carvelli:** Conceptualization, Methodology, Formal analysis, Validation, Visualization, Writing – review & editing. **Wolfgang Kunther:** Conceptualization, Methodology, Data curation, Formal analysis, Investigation, Writing – review & editing. **Mirja Illikainen:** Resources, Writing – review & editing, Supervision, Funding acquisition. **Paivo Kinnunen:** Validation, Resources, Supervision, Writing – review & editing, Funding acquisition.

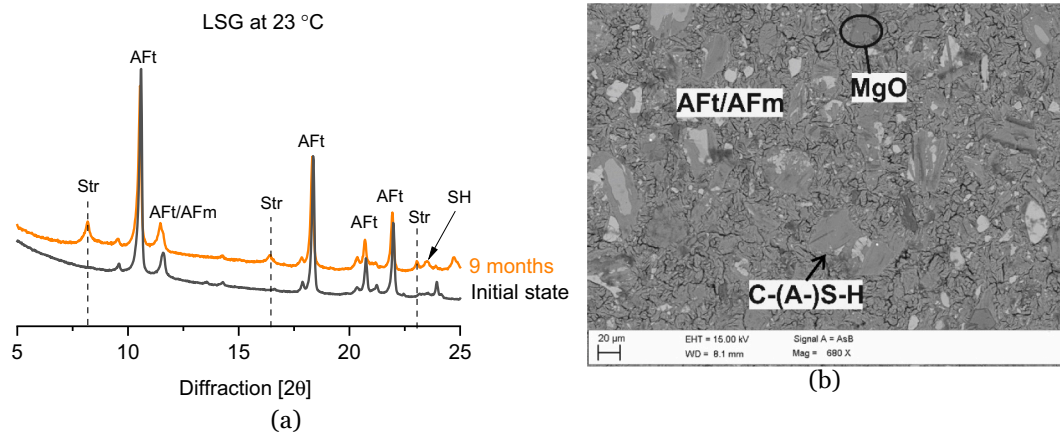### Declaration of competing interest

The authors declare that they have no known competing financial interests or personal relationships that could have appeared to influence the work reported in this paper.
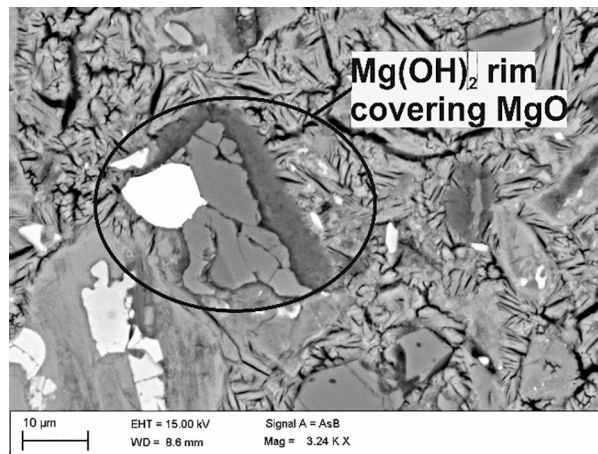
Appendix A

Fig. A1. (a) XRD diffractograms and (b) microstructure of LSG paste after 9 months at the ambient temperature in a water-saturated condition. MgO stayed unreactive and the matrix was sound, while strätlingite was found in LSG paste after 9 months.

Fig. A2. Microstructure of LSG aged at 40 °C after 4 months in water showing the lower reaction kinetics of f-MgO in the binder to form brucite compared to the samples aged at 60 °C in the same period.
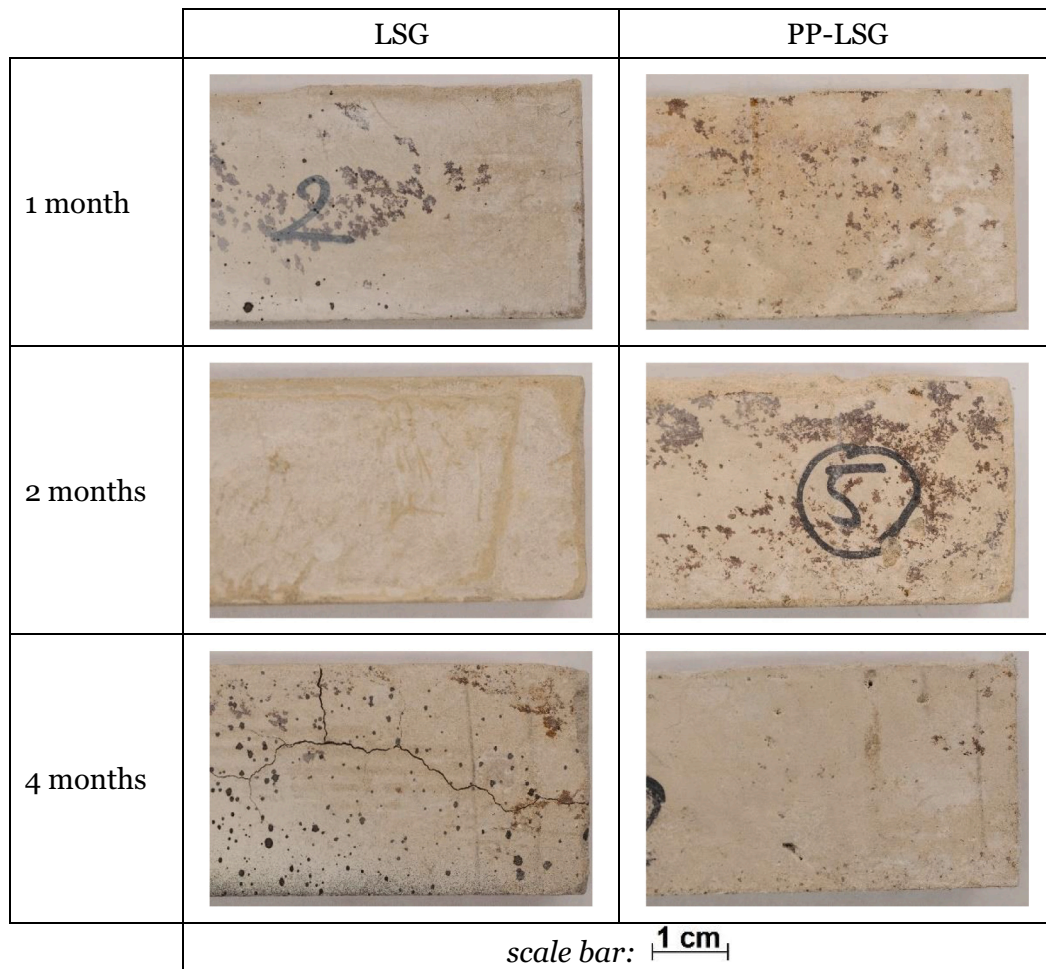
Fig. A3. Sample appearance of LSG and PP-LSG after 1, 2, and 4 months aging at 40 °C in water. Note that there was no change observed by naked eyes on plain and reinforced samples aged at 23 °C in all periods.
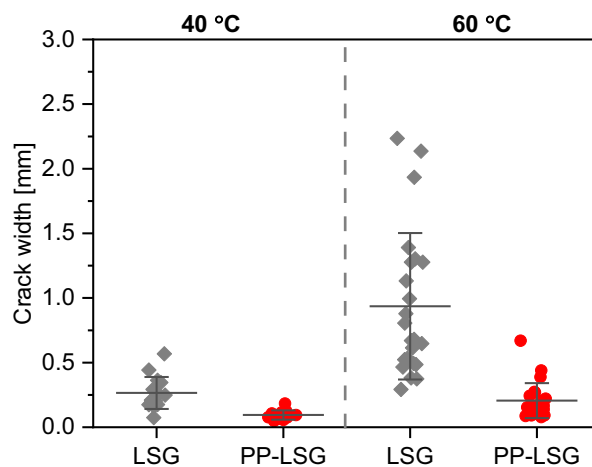

Fig. A4. The width and distribution of cracks appeared in plain LSG and PP-LSG after 4 months of aging at 40 and 60 °C. Note that there was no crack observed in samples aged at other periods. Data was obtained from the processing of digital images of samples in ImageJ.

The porosity of materials was measured with mercury intrusion porosimetry using an AutoPore IV 9500 (Micromeritics, Italy) up to a maximal pressure of ca. 400 MPa. Mortar samples were stopped hydration by solvent exchange for 7 days and dried at ca. 40 °C for 1 day prior to the measurements. The calculation used Washburn equation considering a contact angle of 130° and a surface tension of 0.485 N/m. Fig. A5 shows the total percolated pore volume and the distribution of pore entry radius. The PP-LSG had higher total pore volume than the plain LSG as a result of incorporating fibers in the matrix and this formed a fiber/matrix interfacial transition zone in the material. Additionally, the composite showed a slight decrease in critical pore entry radius compared with the plain material.
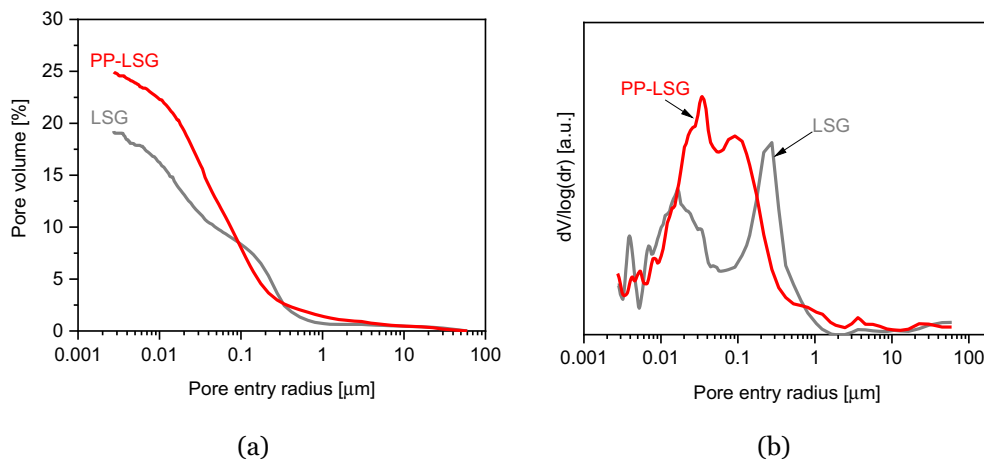
Fig. A5. (a) Cumulative pore volumes and (b) first derivatives of the cumulative curves of unaged LSG and PP-LSG.

References

[1] M.C.G. Juenger, F. Winnefeld, J.L. Provis, J.H. Ideker, Advances in alternative cementitious binders, in: Conf. Spec. Cem. Hydration Kinet. Model. Quebec City 2009 CONMOD10 Lausanne 2010 41, 2011, pp. 1232–1243, https://doi.org/10.1016/j.cemconres.2010.11.012.

[2] E. Gartner, T. Sui, Alternative cement clinkers, Cem. Concr. Res. 114 (2018) 27–39, https://doi.org/10.1016/j.cemconres.2017.02.002.

[3] K.L. Scrivener, V.M. John, E.M. Gartner, Eco-efficient cements: potential economically viable solutions for a low-CO2 cement-based materials industry, Cem. Concr. Res. 114 (2018) 2–26, https://doi.org/10.1016/j.cemconres.2018.03.015.

[4] T. Hanein, J.-L. Galvez-Martos, M.N. Bannerman, Carbon footprint of calcium sulfoaluminate clinker production, J. Clean. Prod. 172 (2018) 2278–2287, https://doi.org/10.1016/j.jclepro.2017.11.183.

[5] A. Klein, G.E. Troxell, Studies of calcium sulfoaluminate admixtures for expansive cements, Proc ASTM. 58 (1958) 986–1008.

[6] L. Zhang, M. Su, Y. Wang, Development of the use of sulfo- and ferroaluminate cements in China, Adv. Cem. Res. 11 (1999) 15–21, https://doi.org/10.1680/adcr.1999.11.1.15.

[7] H. Kühl, Verfahren zur Herstellung von Zement aus Hochofenschlacke, Ger. Pat. (1908), 237777.

[8] H. Nguyen, P. Kinnunen, K. Gijbels, V. Carvelli, H. Sreenivasan, A.M. Kantola, V.-V. Telkki, W. Schroeyers, M. Illikainen, Ettringite-based binder from ladle slag and gypsum – the effect of citric acid on fresh and hardened state properties, Cem. Concr. Res. 123 (2019) 105800, https://doi.org/10.1016/j.cemconres.2019.105800.

[9] K. Gijbels, H. Nguyen, P. Kinnunen, W. Schroeyers, Y. Pontikes, S. Schreurs, M. Illikainen, Feasibility of incorporating phosphogypsum in ettringite-based binder from ladle slag, J. Clean. Prod. 237 (2019) 117793, https://doi.org/10.1016/j.jclepro.2019.117793.

[10] H. Nguyen, P. Kinnunen, V. Carvelli, M. Mastali, M. Illikainen, Strain hardening polypropylene fiber reinforced composite from hydrated ladle slag and gypsum, Compos. Part B Eng. 158 (2019) 328–338, https://doi.org/10.1016/j.compositesb.2018.09.056.

[11] H. Nguyen, M. Staudacher, P. Kinnunen, V. Carvelli, M. Illikainen, Multi-fiber reinforced ettringite-based composites from industrial side streams, J. Clean. Prod. 211 (2019) 1065–1077, https://doi.org/10.1016/j.jclepro.2018.11.241.

[12] C.W. Hargis, B. Lothenbach, C.J. Müller, F. Winnefeld, Carbonation of calcium sulfoaluminate mortars, Cem. Concr. Compos. 80 (2017) 123–134, https://doi.org/10.1016/j.cemconcomp.2017.03.003.

[13] L. Zhang, F.P. Glasser, Investigation of the microstructure and carbonation of CS̄A-based concretes removed from service, Cem. Concr. Res. 35 (2005) 2252–2260, https://doi.org/10.1016/j.cemconres.2004.08.007.

[14] H. Justnes, J. Skocek, T.A. Østnor, C.J. Engelsen, O. Skjølsvold, Microstructural changes of hydrated cement blended with fly ash upon carbonation, Cem. Concr. Res. 137 (2020) 106192, https://doi.org/10.1016/j.cemconres.2020.106192.

[15] J. Bizzozero, C. Gosselin, K.L. Scrivener, Expansion mechanisms in calcium aluminate and sulfoaluminate systems with calcium sulfate, Cem. Concr. Res. 56 (2014) 190–202, https://doi.org/10.1016/j.cemconres.2013.11.011.

[16] C.W. Hargis, B. Lothenbach, C.J. Müller, F. Winnefeld, Further insights into calcium sulfoaluminate cement expansion, Adv. Cem. Res. 31 (2018) 160–177, https://doi.org/10.1680/jadcr.18.00124.

[17] F. Bullerjahn, D. Schmitt, M. Ben Haha, Effect of raw mix design and of clinkering process on the formation and mineralogical composition of (ternesite) belite calcium sulphoaluminate ferrite clinker, Cem. Concr. Res. 59 (2014) 87–95, https://doi.org/10.1016/j.cemconres.2014.02.004.

[18] E.B. da Costa, E.D. Rodríguez, S.A. Bernal, J.L. Provis, L.A. Gobbo, A.P. Kirchheim, Production and hydration of calcium sulfoaluminate-belite cements derived from aluminium anodising sludge, Constr. Build. Mater. 122 (2016) 373–383, https://doi.org/10.1016/j.conbuildmat.2016.06.022.

[19] V. Isteri, K. Ohenoja, T. Hanein, H. Kinoshita, P. Tanskanen, M. Illikainen, T. Fabritius, Production and properties of ferrite-rich CSAB cement from metallurgical industry residues, Sci. Total Environ. 712 (2020) 136208, https://doi.org/10.1016/j.scitotenv.2019.136208.

[20] L. Mo, M. Deng, M. Tang, A. Al-Tabbaa, MgO expansive cement and concrete in China: past, present and future, Cem. Concr. Res. 57 (2014) 1–12, https://doi.org/10.1016/j.cemconres.2013.12.007.

[21] M.R. Nokken, Expansion of MgO in cement pastes measured by different methods, Mater. J. 107 (2010) 80–84, https://doi.org/10.14359/51663469.

[22] G.W. Scherer, Stress from crystallization of salt, Cem. Concr. Res. 34 (2004) 1613–1624, https://doi.org/10.1016/j.cemconres.2003.12.034.

[23] R.J. Flatt, G.W. Scherer, Thermodynamics of crystallization stresses in DEF, Cem. Concr. Res. 38 (2008) 325–336, https://doi.org/10.1016/j.cemconres.2007.10.002.

[24] W. Kunther, B. Lothenbach, J. Skibsted, Influence of the Ca/Si ratio of the C–S–H phase on the interaction with sulfate ions and its impact on the ettringite crystallization pressure, Cem. Concr. Res. 69 (2015) 37–49, https://doi.org/10.1016/j.cemconres.2014.12.002.

[25] W. Kunther, B. Lothenbach, K.L. Scrivener, On the relevance of volume increase for the length changes of mortar bars in sulfate solutions, Cem. Concr. Res. 46 (2013) 23–29, https://doi.org/10.1016/j.cemconres.2013.01.002.

[26] S. Chatterji, Mechanism of expansion of concrete due to the presence of dead-burnt CaO and MgO, Cem. Concr. Res. 25 (1995) 51–56, https://doi.org/10.1016/0008-8846(94)00111-B.

[27] J. Kaufmann, F. Winnefeld, B. Lothenbach, Stability of ettringite in CSA cement at elevated temperatures, Adv. Cem. Res. 28 (2016) 251–261, https://doi.org/10.1680/jadcr.15.00029.

[28] Y. Jeong, C.W. Hargis, H. Kang, S.-C. Chun, J. Moon, The effect of elevated curing temperatures on high Ye'elimite calcium Sulfoaluminate cement mortars, Materials. 12 (2019) 1072, https://doi.org/10.3390/ma12071072.

[29] H. Kabir, R.D. Hooton, N.J. Popoff, Evaluation of cement soundness using the ASTM C151 autoclave expansion test, Cem. Concr. Res. 136 (2020) 106159, https://doi.org/10.1016/j.cemconres.2020.106159.

[30] F. Georget, W. Wilson, K.L. Scrivener, edxia: Microstructure characterisation from quantified SEM-EDS hypermaps, Cem. Concr. Res. 141 (2021) 106327, https://doi.org/10.1016/j.cemconres.2020.106327.

[31] T. Robitaille, C. Beaumont, P. Qian, M. Borkin, A. Goodman, glueviz v0.13.1: multidimensional data exploration, Zenodo (2017), https://doi.org/10.5281/zenodo.1237692.

[32] D.A. Kulik, T. Wagner, S.V. Dmytrieva, G. Kosakowski, F.F. Hingerl, K. V. Chudnenko, U.R. Berner, GEM-Selektor geochemical modeling package: revised algorithm and GEMS3K numerical kernel for coupled simulation codes, Comput. Geosci. 17 (2013) 1–24, https://doi.org/10.1007/s10596-012-9310-6.

[33] GEM Software Main Page, (n.d.). http://gems.web.psi.ch/ (November 19, 2019).

[34] B. Lothenbach, D.A. Kulik, T. Matschei, M. Balonis, L. Baquerizo, B. Dilnesa, G. D. Miron, R.J. Myers, Cemdata18: a chemical thermodynamic database for hydrated Portland cements and alkali-activated materials, Cem. Concr. Res. 115 (2019) 472–506, https://doi.org/10.1016/j.cemconres.2018.04.018.

[35] W. Kunther, Z. Dai, J. Skibsted, Thermodynamic modeling of hydrated white Portland cement–metakaolin–limestone blends utilizing hydration kinetics from 29Si MAS NMR spectroscopy, Cem. Concr. Res. 86 (2016) 29–41, https://doi.org/10.1016/j.cemconres.2016.04.012.

[36] ASTM International, ASTM C494, Standard Specification for Chemical Admixtures for Concrete, ASTM International, West Conshohocken, PA, 2017. www.astm.org.

[37] ISO Committee, ISO 14125:1998, Fibre-Reinforced Plastic Composites – Determination of Flexural Properties, ISO Committee, Geneva, 2013. https://www.iso.org/standard/23637.html.

[38] European Standard, EN 196-1, Methods of Testing Cement - Part 1: Determination of Strength, European Committee for Standardization, 1040 Brussels, Belgium, 2016.

[39] LaVision, LaVision StrainMaster, (2016). http://www.lavision.de/en/products/strainmaster/index.php (accessed January 27, 2017).

[40] F. Bullerjahn, M. Zajac, M. Ben Haha, CSA raw mix design: effect on clinker formation and reactivity, Mater. Struct. 48 (2015) 3895–3911, https://doi.org/10.1617/s11527-014-0451-z.

[41] J. Beaudoin, I. Odler, 5 - Hydration, setting and hardening of Portland cement, in: P.C. Hewlett, M. Liska (Eds.), Leas Chem. Cem. Concr., Fifth Ed, Butterworth-Heinemann, 2019, pp. 157–250, https://doi.org/10.1016/B978-0-08-100773-0.00005-8.

[42] D. Herfort, D.E. Macphee, 3 - Components in Portland cement clinker and their phase relationships, in: P.C. Hewlett, M. Liska (Eds.), Leas Chem. Cem. Concr., Fifth ed., Butterworth-Heinemann, 2019, pp. 57–86, https://doi.org/10.1016/B978-0-08-100773-0.00003-4.

[43] F. Bullerjahn, M. Zajac, M. Ben Haha, K.L. Scrivener, Factors influencing the hydration kinetics of ye'elimite; effect of mayenite, Cem. Concr. Res. 116 (2019) 113–119, https://doi.org/10.1016/j.cemconres.2018.10.026.

[44] H. Nguyen, W. Kunther, K. Gijbels, P. Samyn, V. Carvelli, M. Illikainen, P. Kinnunen, On the retardation mechanisms of citric acid in ettringite-based binders, Cem. Concr. Res. 140 (2021) 106315, https://doi.org/10.1016/j.cemconres.2020.106315.

[45] H. Nguyen, P. Kinnunen, V. Carvelli, M. Illikainen, Durability of ettringite-based composite reinforced with polypropylene fibers under combined chemical and physical attack, Cem. Concr. Compos. 102 (2019) 157–168, https://doi.org/10.1016/j.cemconcomp.2019.04.021.

[46] J. Nam, G. Kim, B. Lee, R. Hasegawa, Y. Hama, Frost resistance of polyvinyl alcohol fiber and polypropylene fiber reinforced cementitious composites under freeze thaw cycling, Compos. Part B Eng. 90 (2016) 241–250, https://doi.org/10.1016/j.compositesb.2015.12.009.

[47] H.-D. Yun, K. Rokugo, Freeze-thaw influence on the flexural properties of ductile fiber-reinforced cementitious composites (DFRCCs) for durable infrastructures, Cold Reg. Sci. Technol. 78 (2012) 82–88, https://doi.org/10.1016/j.coldregions.2012.02.002.

[48] E.-H. Yang, S. Wang, Y. Yang, V.C. Li, Fiber-bridging constitutive law of engineered cementitious composites, J. Adv. Concr. Technol. 6 (2008) 181–193, https://doi.org/10.3151/jact.6.181.

[49] B. Felekoğlu, K. Tosun-Felekoğlu, M. Keskinateş, E. Gödek, A comparative study on the compatibility of PVA and HTPP fibers with various cementitious matrices under flexural loads, Constr. Build. Mater. 121 (2016) 423–428, https://doi.org/10.1016/j.conbuildmat.2016.06.004.

[50] V.C. Li, A simplified micromechanical model of compressive strength of fiber-reinforced cementitious composites, in: Spec. Issue Micromechanics Fail. Cem. Compos. 14, 1992, pp. 131–141, https://doi.org/10.1016/0958-9465(92)90006-H.

[51] EN 1992-1-1:2004, Eurocode 2: Design of concrete structures - Part 1-1: General rules and rules for buildings, CEN (European Committee for Standardization), Brussels, Belgium, 2004.